

## ARTICLE OPEN



# Rotating square tessellations enabled stretchable and adaptive curved display

Yang Deng<sup>1,3</sup>, Kuaile Xu<sup>2,3</sup>, Rui Jiao<sup>1</sup>, Weixuan Liu<sup>2</sup>, Yik Kin Cheung<sup>1</sup>, Yongkai Li<sup>1</sup>, Xiaoyi Wang<sup>1</sup>, Yue Hou<sup>1</sup>, Wei Hong<sup>1,2</sup> and Hongyu Yu<sup>1</sup><sup>✉</sup>

Curved displays can adjust their shape to accommodate different objects and are used in electronics and decorative lighting. Due to the immutable pixel spacing, existing commercial curved displays are flexible but not compatible with undevelopable surfaces. Inspired by kirigami and auxetic structures, we propose an approach that combines luminescent elements and rotating square tessellations to create a stretchable, arbitrary curve adaptive display. We connect square islands by vertical interconnects to relieve the stress concentration and provide extra deformation patterns. The vertical interconnects are patterned on a flexible printed circuit board (FPCB) using laser cutting and folded up via specially designed molds. Further, the freed-up space by folded interconnects allows the structure to be compressed. A prototype stretchable display is demonstrated that it can maintain electrical performance under biaxial strain and adapt to different Gaussian curvature surfaces, including cylindrical, spherical, saddle and arbitrary surfaces. Theoretical models and finite element calculations are established to describe the tensile behavior of the structures under different boundary conditions and agree with the experimental results. This proposed technology paves a feasible solution of mass production of adaptive curved displays and sets the trend for the next-generation display.

*npj Flexible Electronics* (2024)8:4; <https://doi.org/10.1038/s41528-023-00291-y>

## INTRODUCTION

While planar displays remain the dominant form of displays, emerging applications, from wearable devices<sup>1</sup>, smart skin<sup>2,3</sup> to curved optics, soft robotics<sup>4,5</sup>, and home embellishment, require three-dimensional curved structures<sup>6–8</sup>. Consequently, curved displays have gained popularity as one of next-generation display technologies that combines functionality and attractivity. With consumers' ever-increasing demand for both aesthetics and practicality, curved displays have seen a recent surge in development.

Bending has been a widely used method to realize curved displays<sup>9</sup>. Flexible display production technology has matured and is currently utilized in various electronic devices, lighting, billboards, etc. Typically, organic light-emitting diode (OLED) displays in foldable smartphones are a prime example of the rapid development of flexible displays<sup>10</sup>. However, planar-substrate-based flexible displays are intrinsically incompatible with non-developable surfaces. It has been shown from fundamental theorems of differential geometry that the Gaussian curvature remains invariant in isometric transformations<sup>11,12</sup>. As a result, flexible but non-stretchable planar displays can only be bent into developable surfaces, such as tubes or cones.

In line with the methodologies for stretchable or its enabled curved electronics in general, several methods exist to make a display stretchable. Formerly, the dominant scheme was to mount rigid components onto an elastic substrate<sup>13</sup>, or to connect rigid islands with stretchable interconnects to achieve global stretchability<sup>14,15</sup>. However, due to the low stiffness and short fatigue life of stretchable materials (e.g. polydimethylsiloxane (PDMS), Ecoflex, dragon skin, PEDOT)<sup>16</sup>, the luminescent or conductive materials embedded in them are prone to damage. For example, Larson et al.<sup>17</sup> reported a stretchable capacitive display driven by

AC. The ZnS phosphors were embedded in Eco-Flex and sandwiched in electrodes made of elastic matrix (polyacrylamide, PAM). The phosphors emit light when an AC voltage is applied to the electrode. Unfortunately, because the silicone and hydrogel undergo large deformation under tension, the density of the phosphors decreases and even cracks occur, leading to device failure. Another feasible strategy is to connect rigid islands of illuminant elements with geometrically stretchable interconnections. Rogers et al.<sup>18</sup> developed a technique to connect the  $\mu$ -ILED array using serpentine interconnects and then transfer to 400  $\mu$ m thick pre-stretched PDMS slices and achieve 48% stretchability. In addition, Tripathi et al.<sup>19</sup> reported a 32  $\times$  32 AMLED stretchable display connected with 2 mm long horseshoe metal interconnects. However, such displays based on stretchable interconnects often rely on elastic material as the substrate, which creates limitations similar to those described above. In addition, stretchable interconnects expose the shortcomings of complex structure, difficult manufacturing and high cost, which are not conducive to mass production.

Lately, some original schemes have emerged to implement stretchable or curved displays<sup>20–22</sup>. Xiang et al.<sup>23</sup> reported that the display textiles woven from conductive weft and luminescent warp fibers present flexibility, water resistance, and interaction function, etc. However, the degradation of organic materials (such as electroluminescence materials) used in displays still exists. Besides, Orderly arranged sub-pixels (RGB) are indispensable for colorful display (such as mainstream PenTile and Delta arrangement for OLED)<sup>24</sup>, while the weft-warp arranged electroluminescent units almost obliterates the potential for achieving colorful display textiles. Deng et al.<sup>25</sup> proposed a scheme combining programmed origami tessellations with LED chips to realize a curved display. They optimized the original Miura-origami pattern

<sup>1</sup>Department of Mechanical and Aerospace Engineering, Hong Kong University of Science and Technology, Kowloon, Hong Kong SAR 999077, China. <sup>2</sup>Shenzhen Key Laboratory of Soft Mechanics & Smart Manufacturing, Department of Mechanics and Aerospace Engineering, Southern University of Science, Technology, Shenzhen, Guangdong 518055, China. <sup>3</sup>These authors contributed equally: Yang Deng, Kuaile Xu. <sup>✉</sup>email: hongw@sustech.edu.cn; hongyuyu@ust.hk

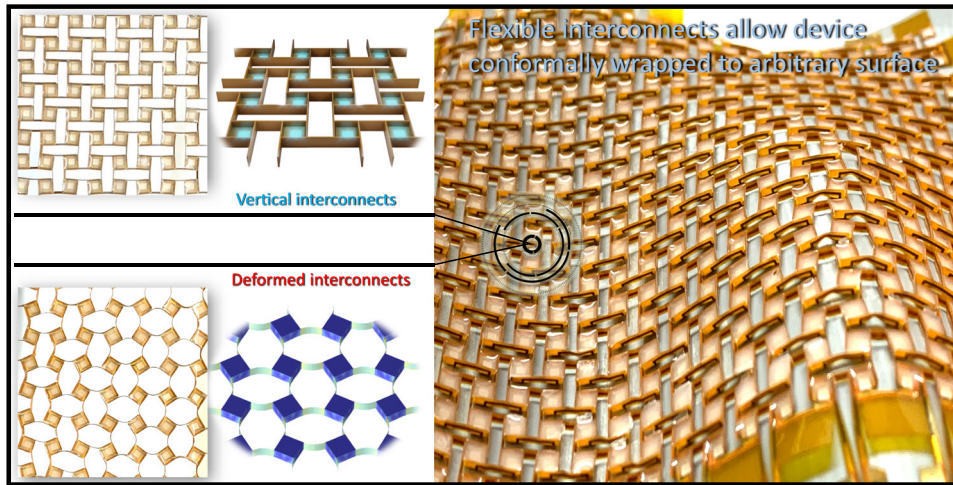


**Fig. 1** Adaptive curved display with rotating-square-based auxetic structure.

by entitling the vertexes extra degrees of freedom to design tessellation patterns and folded it into the desired shapes with minimum total potential energy. Unfortunately, the display fabricated by MEMS-based process is inadequate for the larger curved surface.

Auxetics<sup>26</sup>, known as the structure or materials with negative Poisson's ratio, has been studied geometrically and mechanically for decades since the 1980s<sup>27–30</sup>. Various cut units that make up 2D auxetic structures have been developed, including rectangles, triangles, hexagons, stars, and their hybrids, etc. Typically, the auxetic structure composed of square tessellations has the potential to fabricate stretchable display due to its regular structure and homogeneous global deformation when stretched. However, traditional auxetic structures consisting of rotating units are often damaged due to the enormous strains at rigid nodes, which obliterates the possibility of laying circuits<sup>22</sup>. Further, to achieve higher stretchability of the kirigami-based auxetic metastructures, Tang et al.<sup>31</sup> designed the geometry and structure of the cut units by combining the line cut, cut-out, and hierarchy of the structure, which dramatically improved its stretchability. However, line cut can only produce stretchable metastructures. The incompressibility beyond their inherent cut structure will restrict their potential applications in electronics, where stretchability and compressibility are often required for functionality.

In this study, inspired by kirigami-based auxetic metastructures, we propose a concept to fabricate a stretchable and adaptive curved display by integrating thin vertical interconnects connected rotating squares and LED chips (shown in Fig. 1). Thin vertical interconnects overcome the inability to pattern circuits at rigid nodes, and the space they free up allows the rotating squares to be compressible (layout and schematic diagram shown in Fig. 2a, b). We constructed the matrix circuit on an ultra-thin FPCB and patterned the vertical interconnects layout by laser cutting. Surface mount technology (SMT) was used to place illuminant elements onto the FPCB and the molds guidance process was used to fold planar interconnects into the vertical configuration. After encapsulation, the display can be locally stretched or compressed to match the surface with different Gaussian curvature adaptively owing to vertical interconnects distortion. Digital image correlation (DIC) and 3D finite element method (FEM) model of rotating square structure were used to analyze its local and global mechanical behavior and geometrical morphology under tension. It presents that the introduction of vertical interconnects into rotating square tessellations dramatically reduces the stress concentration effect and improves the adaptability of the structure.

## RESULTS AND DISCUSSION

### The design principles of rotating square tessellations

Here, we explore the design of a generalized square-cut unit in auxetic structures for enhanced stretchability through its rigid-body rotation. Figure 2c shows an auxetic structure with a laser-inscribed pattern, in which orthogonal cuts divide the sheet into  $4 \times 4$  interconnected square islands. As demonstrated in Fig. 2d, e, stretching the auxetic structures uniaxially led to the equal biaxial expansion (up to ~40% in each direction), exhibiting an auxetic behavior with a negative Poisson's ratio. Upon stretching, each square island underwent an in-plane rotation, with the connection at the marked corners (red circle in Fig. 2c) unchanged, to render an expanding structure. When stretching the rotating squares, the cut slots evolved into a uniform array of rhombic holes (red rhombus in Fig. 2d, e).

We now generalize the design by replacing the straight cuts with I-shape cuts (blue lines in Fig. 1a), and pre-fold at the edges of the square islands (along the red dot lines in Fig. 2a). The cutting and folding result in an array of smaller square islands (Fig. 2b). Let us denote the edge length of an island by  $w$ , and the distance between adjacent islands by  $h$ . After folding, the vertical compartments which act as interconnects have a height of  $h/2$ , and length  $l = 2w + h$ . To quantify the usable area in the structure, we define the area utilization ratio as that between the in-plane components (the square islands) and the total area of the original sheet before cutting:

$$R = \frac{N_x w \times N_y w}{[N_x w + (N_x - 1)h] \times [N_y w + (N_y - 1)h]}, \quad (1)$$

where  $N_x$  and  $N_y$  are the numbers of square islands in the X- and Y-directions, respectively. In the following experiment, considering the homogeneity of pixels and the difficulty of FPCB processing and folding, we set  $w = h$  and thus  $l = 3w$ . For example, the structure with  $4 \times 4$  connected squares as shown in Fig. 2 has an area utilization ratio  $R = 33\%$ . By definition, the area utilization ratio depends on  $N_x$ ,  $N_y$ , and the ratio  $w/h$  (details and application in the Supplementary Information). It should also be noted that the height of the interconnects and consequently the area utilization ratio  $R$  can be varied in general.

Figure 2f–h present the schematic diagrams and photos (insets) of the constrictive, original, and extended states of the rotating-square auxetic structure, respectively. Limited by the spacing  $b$  between adjacent square islands, the structure cannot be further compressed when the vertices of the islands are in contact (Fig. 2f), unless the interconnects buckle. At this point, the spaces between neighboring islands take the shape of two connected

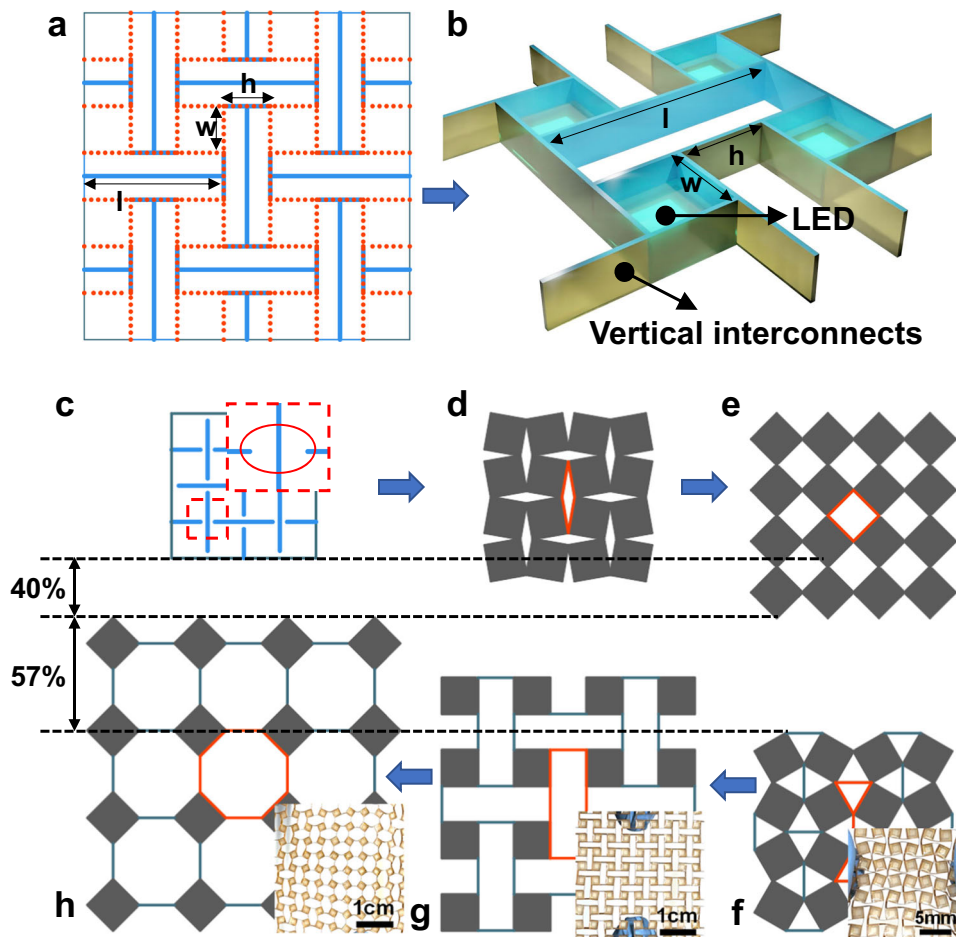


**Fig. 2 Design concept of rotating-square-based auxetic structure.** **a** The layout of prescribed cuts for vertical interconnects connected squares and the red dot lines suggest the creases after folded. **b** schematic diagram of the structure. **c**  $4 \times 4$  connected square islands from patterned cuts. **d, e** Configurations of the structure upon rotation of the square islands by  $10^\circ$  and  $45^\circ$ , respectively. **f–h** The schematics of the constrictive, original, and extended configurations. Insets: photos of the compressed, original, and stretched states of a display based on the mechanism.

equilateral triangles. Analogously, an extension limit is reached when the islands rotate by  $45^\circ$  and the interconnects are all aligned in horizontal or vertical direction, and the inter-island spaces deform into octagons (Fig. 2h). This  $4 \times 4$  auxetic structure expands by  $\sim 57\%$  biaxially from the constrictive to the extended configuration. The stretchability of the proposed structure is discussed detailedly in the Supplementary Information.

#### FPCB design and folding scheme

Figure 3a presents a schematic of  $2 \times 2$  pixels and FPCB stack-up in an exploded view. The BXDA 40 mil  $\times$  40 mil LED chip (Bridgelux) is configured onto a  $\sim 17\ \mu\text{m}$  solder resist made with epoxy. The contact pads are pre-opened, and the orthogonal hollowed-out gaps are released for creases. Solder resist is used to protect and stiffen the remaining areas of the FPCB so that the exposed region can be folded easily to form creases. The  $12\ \mu\text{m}$  first and second metal circuits are patterned on both sides of the  $30\ \mu\text{m}$  PI film. The pattern and function of the underlying solder resist are the same as described above. Figure 3b shows the general layout of the 2D display consisting of 400 pixels spaced  $2\ \text{mm}$  apart. The partial enlargement (marked by a black box) presents the details of the composition of a pixel and its surroundings, including the I-shaped cuts, the reserved  $300\text{-}\mu\text{m}$ -wide creases (red dotted lines,  $2\ \text{mm}$  apart between center lines), the solder resist layout

(orange rectangles marked by brown dotted lines) and the LED chip. Figure 3c–e respectively show the schematics of folding, packaging and demolding processes of a single rotating square. Initially, the 1st mold with a stubby square column presses the square functional area on the planar FPCB into the reserved square groove (2nd mold). Simultaneously, the orthogonal cuboid column on the 2nd mold erects the interconnects. The inset optical image shows the FPCB configuration after folded, where the square functional area has trapped in congruent square groove and the vertical interconnects are shaped in orthogonal grooves with a width of  $0.6\ \text{mm}$ . After that, to prevent the detachment of LED chip and, crucially, fix interconnects' morphology to prevent it from bouncing after demolding, automatic dispenser (Camalot 1414) and UV sensitive epoxy resin are needed to encapsulate the chip. Then, 3rd mold with a slender square column is used to push the encapsulated device out of the orthogonal groove through a square through-hole in the center of the 1st mold. Figure 3f shows the optical image of encapsulated display and the partial enlargement, marked by black box, presents cured UV epoxy resin. We precisely controlled the unit dose of UV epoxy resin through the dispenser, so that forms a smooth cuboid after curing, which will be discussed in the following section.

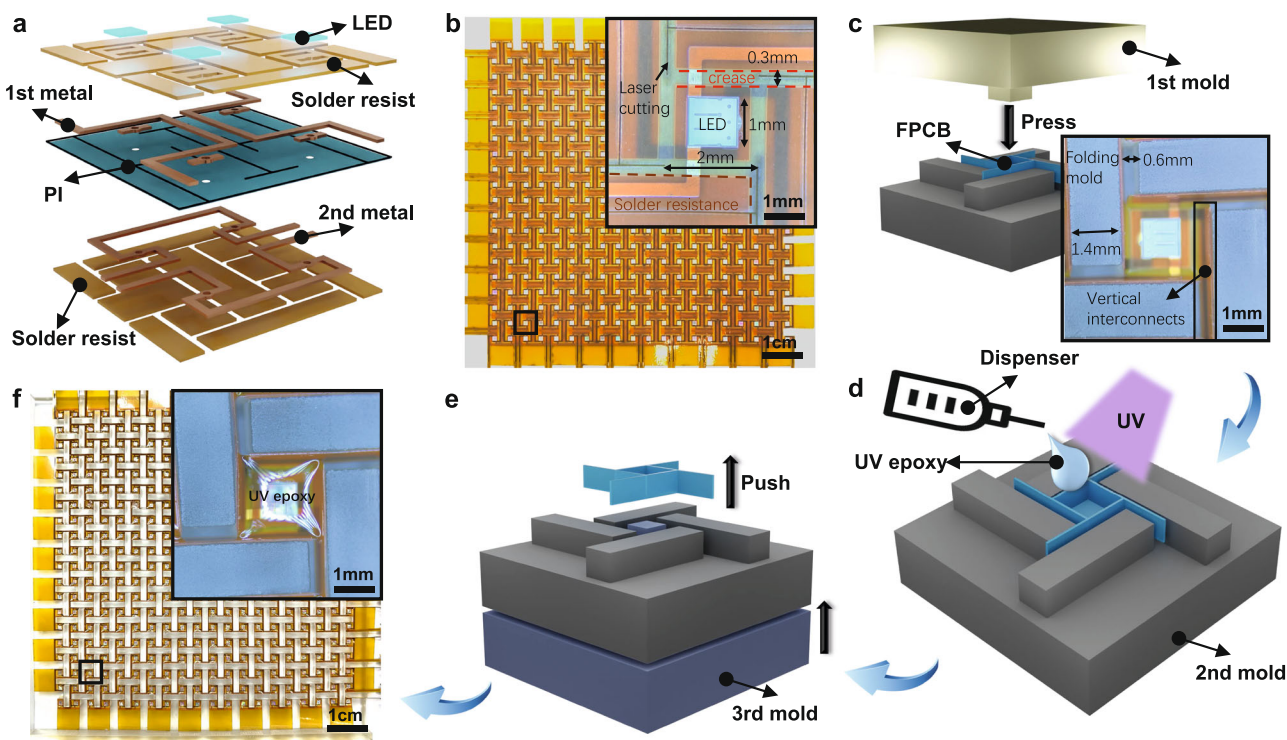


**Fig. 3 Structure and folding process of a stretchable planar display.** **a** Schematic of FPCB stack-up in an exploded view. **b** Photo of 20 × 20 pixels planar display and the partial enlargement of a unit cell. **c–e** Schematics of folding, packaging and demolding processes of a single rotating square. The inset shows a single rotating square trapped in a folding mold. **f** Photo of folded planar display and inset shows the cured UV epoxy cuboid.

### Rotating-square-based curved display

Gaussian curvature, which characterizes the morphology of a surface (convexity and developability), is defined as the function of the product of the two principal curvatures at the points on the surface ( $K = k_1 k_2$ ). Here, we further validated the versatility and fidelity by fitting the rotating square auxetic-structure-based display onto representative cylindrical ( $K = 0$ ), spherical ( $K > 0$ ), saddle ( $K < 0$ ), and irregular surfaces (random  $K$ ). As shown in Fig. 4a, the display is fitted on a cylindrical mold with a 5 cm radius ( $k_1 = 0.2\text{cm}^{-1}$ ,  $k_2 = 0$ ). As can be seen from Fig. 4b, the pixels exhibit homogeneous alignment due to the developability of the cylinder. In contrast, pixels on a spherical surface ( $k_1 = k_2 = 0.2\text{cm}^{-1}$ ) demonstrate local expansion (Fig. 4d) and those on a saddle surface ( $k_1 = -k_2 = 0.2\text{cm}^{-1}$  at the saddle point) exhibit local contraction (Fig. 4g). Particularly, Gaussian curvature changes with the undulating topography of an irregular surface (Fig. 4j), and the pixel layout varies accordingly (Fig. 4k). A passive line scan control system, consisting of shift registers 74HC595 (Texas Instruments), is used to drive the curved display. Photos of the display in operation (showing letter pattern "UST" in Fig. 4c, f, i, and word "HELLO" in Fig. 4l, animation demonstration in Supplementary Movies 1, 2) are demonstrated. In addition, the effects of vertical interconnects on viewing angle and luminance are discussed in detail in the Supplementary Information.

Further, the proposed conformal display can be attached to the surface of soft or flexible subjects, such as balloons and cloth. Owing to its stretchability, the display can tightly cling to objects even when pressed or kneaded, a desired feature for toys or garments. Here, an interactive toy is made for demonstration by attaching the curved display onto an inflated balloon. Five thin film pressure sensors (LEGACT RP-C7.6ST) are pre-attached to the display (as shown in Fig. 5a). Upon detection of pressure, the signal is forwarded to a data collector which sends instructions through the MCU, to present different expressions over the display – the initial smiley face is switched into a sad face when

pressed (Supplementary Movie 3). In addition, the stability and reliability of the display are also demonstrated by kneading the balloon (Supplementary Movie 4), during which the display works stably.

The rotating square structure attracts the attention of flexible electronics manufacturers due to its geometry and mechanical properties. In this paper, we developed a derivative of the rotating square structure connected with vertical interconnects and applied it to the production of adaptive curved displays. We analyzed the properties of this innovative structure, including area utilization and stretchability, and performed morphological and mechanical analyses using DIC methods. Then we introduced the structure to flexible circuit board and combined it with surface mounted technology and molds guidance method to manufacture adaptive curved display prototypes. We tested the prototype's performance and fitted it to different surfaces, including cylinder, sphere, saddle and arbitrary surface. The device demonstrates excellent and stable performance in practical application, which presents the feasibility of auxetic structure applied to electronic products and provides an approach for the innovation of stretchable and curved electronics.

## METHODS

### Morphological and mechanical analyses

To analyze the morphology and mechanical behaviors, the rotating-square structure is simplified into an array of rigid islands connected by inextensible beams of bending stiffness  $EI$ . Utilizing the symmetry and periodicity of the structure, a representative unit consisting of one island and four halves of the interconnects is taken, as shown in Fig. 6a. Here, the edge length of the square island is taken to be  $2l$ , with  $l$  being the half-length of an interconnect. Due to mirror symmetry, the deformation and equivalent boundary conditions of the characteristic unit can be simplified. To model the state of uniaxial tension, a pair of forces  $P$

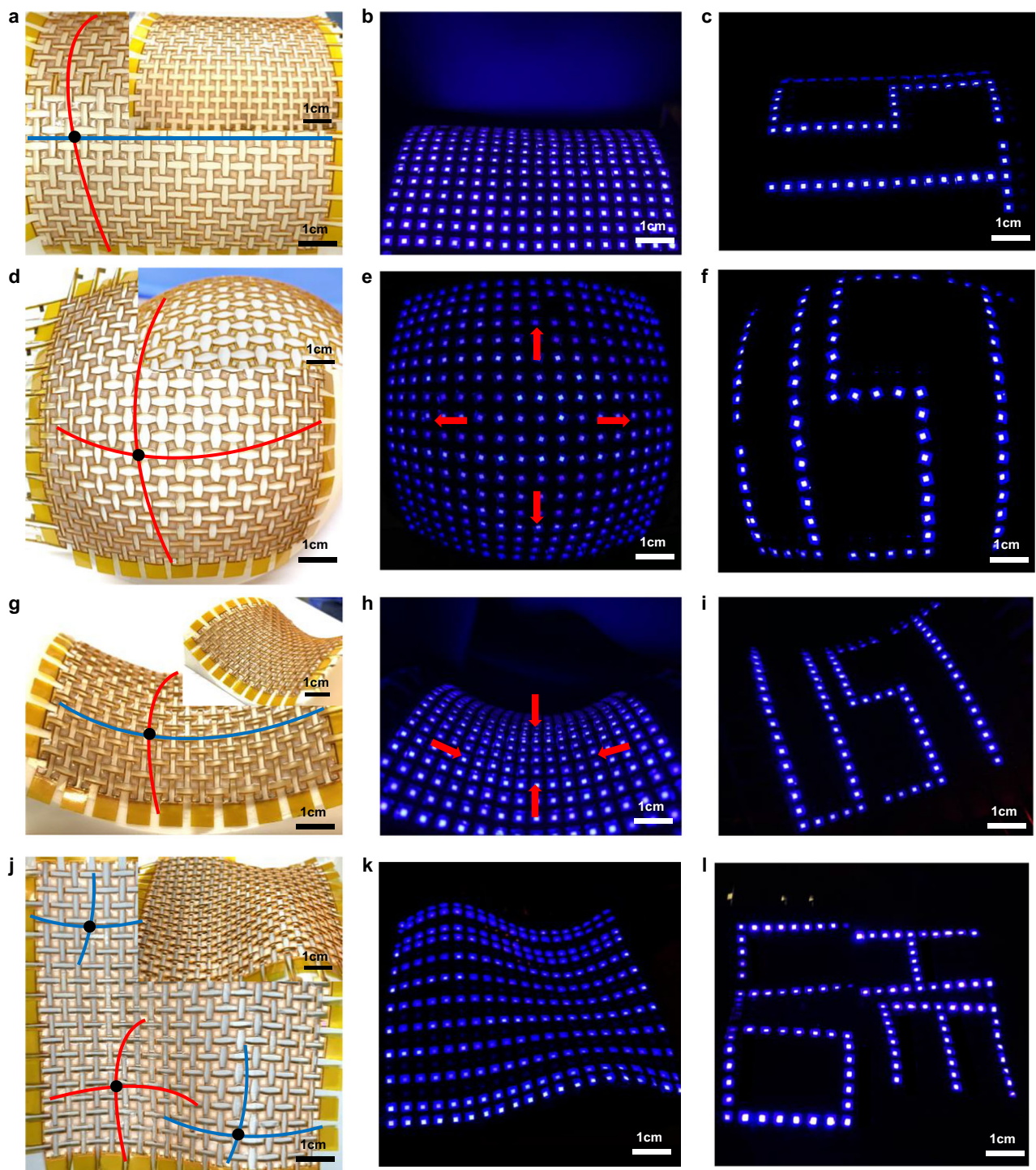


**Fig. 4 Photos of display fit conformally to various 3D curved surfaces and in operation.** **a, d, g, j** Photos of the rotating-square-based display fit to cylindrical, spherical, saddle-shape, and irregular surfaces. **b, e, h** Photos of the curved display with all LEDs lit, and **(k)** Light striation on arbitrary surface. **c, f, i, l** Photos of the display in operation (showing letter pattern “UST” in **c, f** and **i**, and word “HELLO” in **l**). Insets: photos of the curved display at different viewing angles.

is applied on the two half interconnects A and C in the horizontal direction, while the half interconnects B and D are subject to no vertical force. The symmetry requires that all four ends of the half interconnects are rotation-free, resulting in bending moments  $M$  on A and C, and  $M'$  on B and D.

Let  $H$  be the vertical distance between the midpoints of interconnects A and C, and  $H'$  be that between the two corresponding corners of the square island. The vertical deflection

$h$  of each half interconnect is then related to them as  $H = H' - 2h$ . Simple geometric analysis yields the relation  $H' = 2l(\cos \varphi - \sin \varphi)$ , where  $\varphi \in [0, \pi/4]$  is the angle of rotation of the island. The moment balance of the representative cell

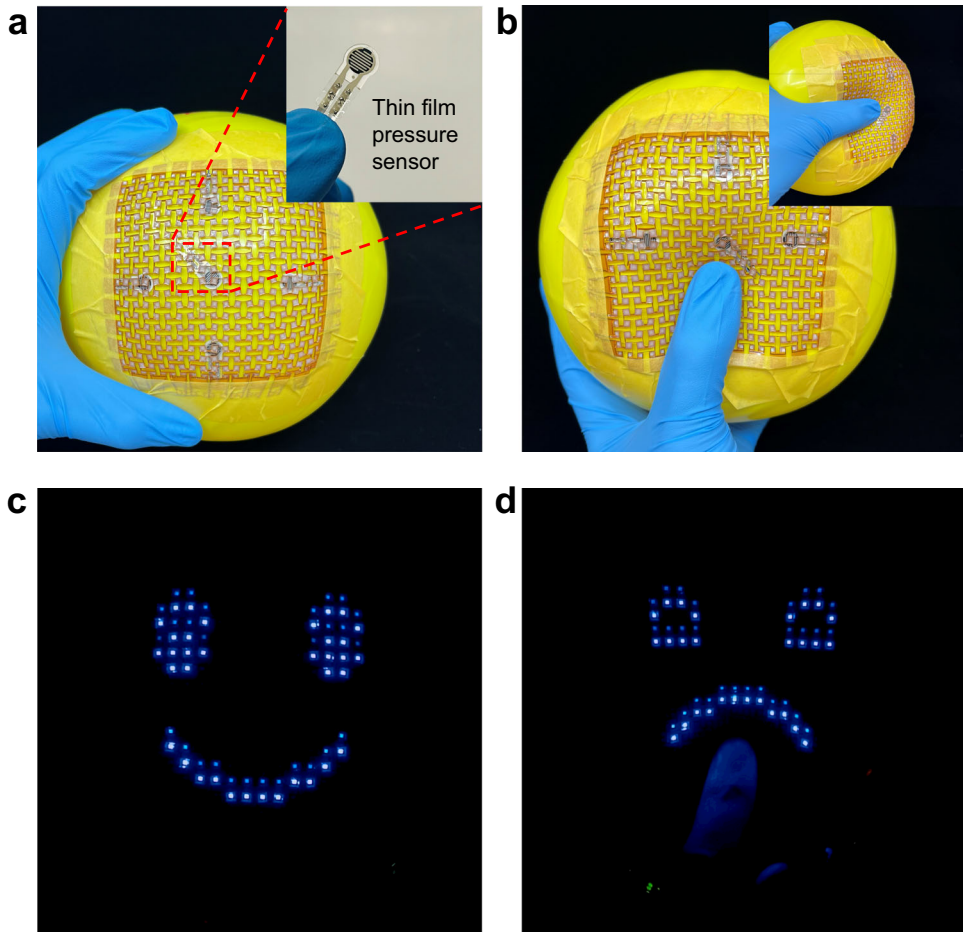


**Fig. 5 Photos of a display fitted on a balloon. **a**** The as-assembled state of the device. **b** The state when the device is pressed with a thumb. **c, d** Different expressions shown on the display corresponding to the states in (a, b).

dictates that

$$P \cdot H = 2(M + M'). \quad (2)$$

Let us first take the small-rotation and small-deformation assumptions. The state of each of the half interconnect is similar to that of a Euler–Bernoulli cantilever beam subject to force and moment at the end. According to the classic mechanics of material, the end deflection should be  $\delta = \frac{P \sin \varphi \beta^3}{3EI} + \frac{M \beta^2}{2EI}$ . The combination of geometric relationship and moment balance leads to

$$(2 + \varphi) \cos \varphi - 5 \sin \varphi + \frac{\beta \sin \varphi \cos \varphi}{6} - \frac{4\varphi}{\beta} = 0, \quad (3)$$

where  $\beta = \frac{P \beta^2}{EI}$  is a dimensionless parameter. The relationship between dimensionless external force  $f = 2\beta$  and  $\varphi$  is shown in Fig. 6b. The average strains of the whole structure under horizontally uniaxial tension are:

$$\varepsilon_x = \cos \varphi + \frac{1}{2} \sin \varphi + \frac{\beta \sin^2 \varphi}{24} + \frac{\varphi \sin \varphi}{4} - 1, \quad (4)$$

$$\varepsilon_y = \frac{1}{2} \left( \cos \varphi + \sin \varphi + \frac{1}{\varphi} \sin \varphi \right) - 1, \quad (5)$$

where  $\varepsilon_x$  is the axial strain and  $\varepsilon_y$  is the lateral strain.

To verify the theoretical model under small rotation and deflection condition, the Poisson's ratio of the structure is derived from the model is compared to experiments. An INSTRON tensile strength tester and digital image correlation (DIC) method was

employed. A 5 mm thick thermoplastic polyurethane (TPU) sheet was prepared and laser cut to create a scaled-up rotating square structure model (Fig. 6d). The sample was clamped at top and bottom. When the external load is relatively small, there is good agreement between theory and experiment as shown in Fig. 6f. However, due to the extra clamping, the Poisson's ratio was found to be distorted after stretching to a certain extent.

As the external load increases, the beams may undergo finite deflection or finite rotation, which exceeds the small deformation assumption. Therefore, we also propose a more accurate model with interconnect considered as inextensible slender rod, which also known as elastica. To name each material particle along the half-interconnect, let  $S$  be the arc distance between a material particle and the end. The balance of moment on the elastica requires that

$$\frac{d}{dS} M(S) + \mathbf{P} \cdot \mathbf{n}(S) = 0, \quad (6)$$

where  $M(S)$  is the moment on each section of the elastica,  $\mathbf{P}$  is the external force in the vector form and  $\mathbf{n}(S)$  is the unit normal vector along the elastica. The constitutive law of the elastica leads to

$$\kappa(S) = \frac{M(S)}{EI}, \quad (7)$$

where  $\kappa = \left| \frac{dn}{ds} \right|$  represents the curvature on the elastica. By considering boundary conditions, we can derive the relation between rotation and external load, in which we use  $\beta = \frac{P \beta^2}{EI}$  and  $\gamma = \frac{M}{P \beta}$  as the dimensionless quantities of force and bending moment on the interconnect C. The relation between rotation

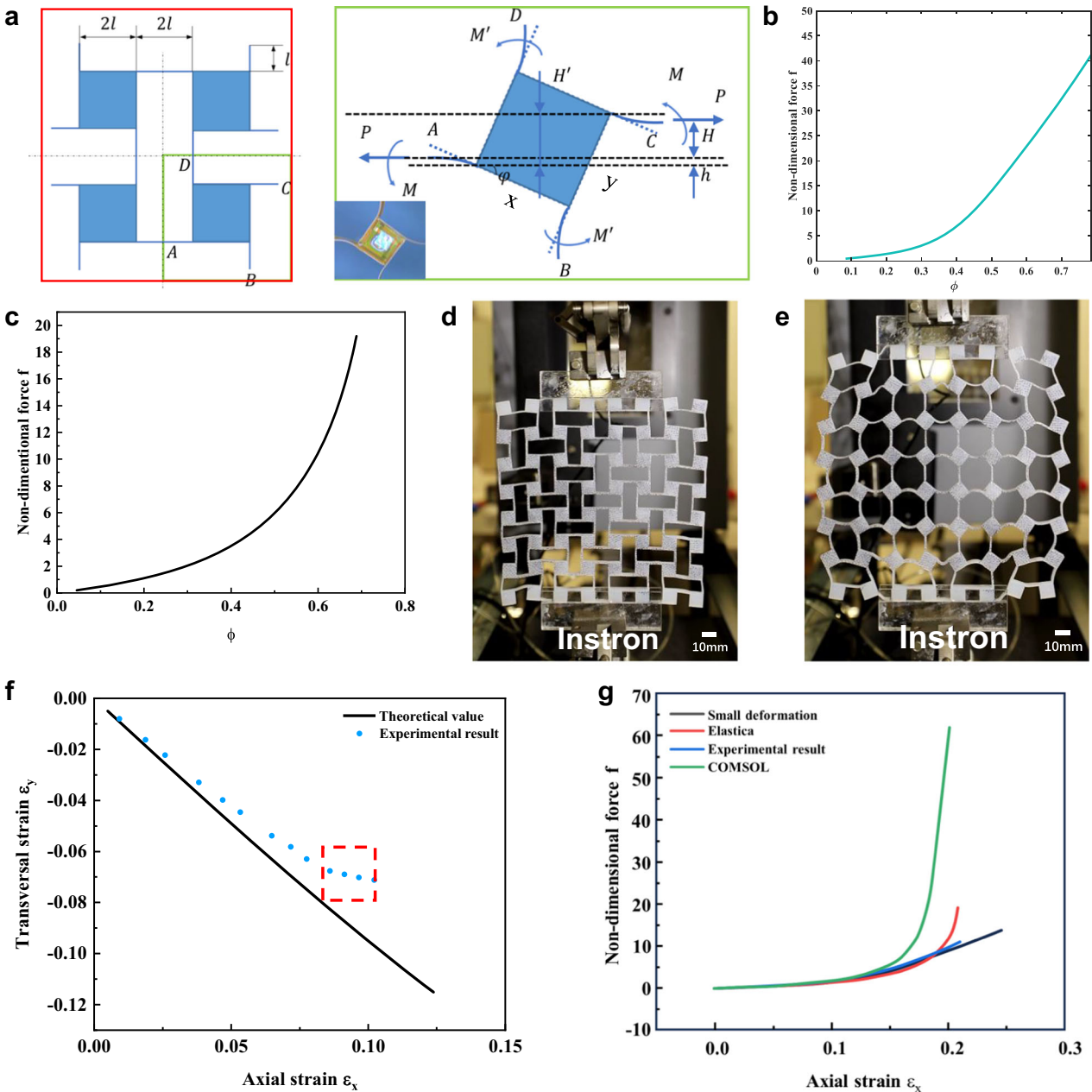


**Fig. 6 Mechanical characterization of the structure.** **a** Representative unit (consisting of four islands as a group) and the free-body diagram of a rotating island. Inset: photo of an island in a structure subject to stretch. **b** Calculated dimensionless force  $f$  as a function of the angle of rotation  $\varphi$  (small deformation). **c** Relationship between the dimensionless force  $f$  and the square island's rotated angle  $\varphi$  (large deformation). **d** Photo of a TPU model clamped for mechanical tests. **e** Photo of the model when fully stretched. **f** Relation between the lateral strain and the axial strain, showing both experimental and theoretical results. **g** Measured dimensionless force-strain curve, in comparison with various theoretical and numerical predictions.

angle of the square island and external load is

$$\varphi = 2am\left(\frac{\beta\gamma}{2} \mid -\frac{4}{\beta\gamma^2}\right), \quad (8)$$

where  $am(\cdot|\cdot)$  represents the Jacobi amplitude function. Also, the end location of the elastica can be obtained by the integral of the unit tangent vector  $\mathbf{t}(S)$  as:

$$\mathbf{r}(S) = \int_0^S \{\mathbf{t}(S) \cdot \mathbf{t}(0), \mathbf{t}(S) \cdot \mathbf{n}(0)\} dS. \quad (9)$$

Then combine the elastica equations with geometric relationship and moment balance, we can obtain the average strains

under inextensible assumption and finite rotation condition:

$$\varepsilon_x = \frac{1}{2}(\cos \varphi + \sin \varphi + \bar{x} \cos \varphi + \bar{y} \sin \varphi) - 1, \quad (10)$$

$$\varepsilon_y = \frac{1}{2}\left(\cos \varphi + \sin \varphi + \frac{1}{\varphi} \sin \varphi\right) - 1 \quad (11)$$

The relationship between  $\varepsilon_x$  and  $f$  (Fig. 6g) can be derived from the above equations. The computational difficulty caused by Jacobian amplitude function can be avoided by Taylor expansion approximation.

Adopting the same design parameters, Fig. 6g plots the dimensionless force-strain curve of small deformation model,

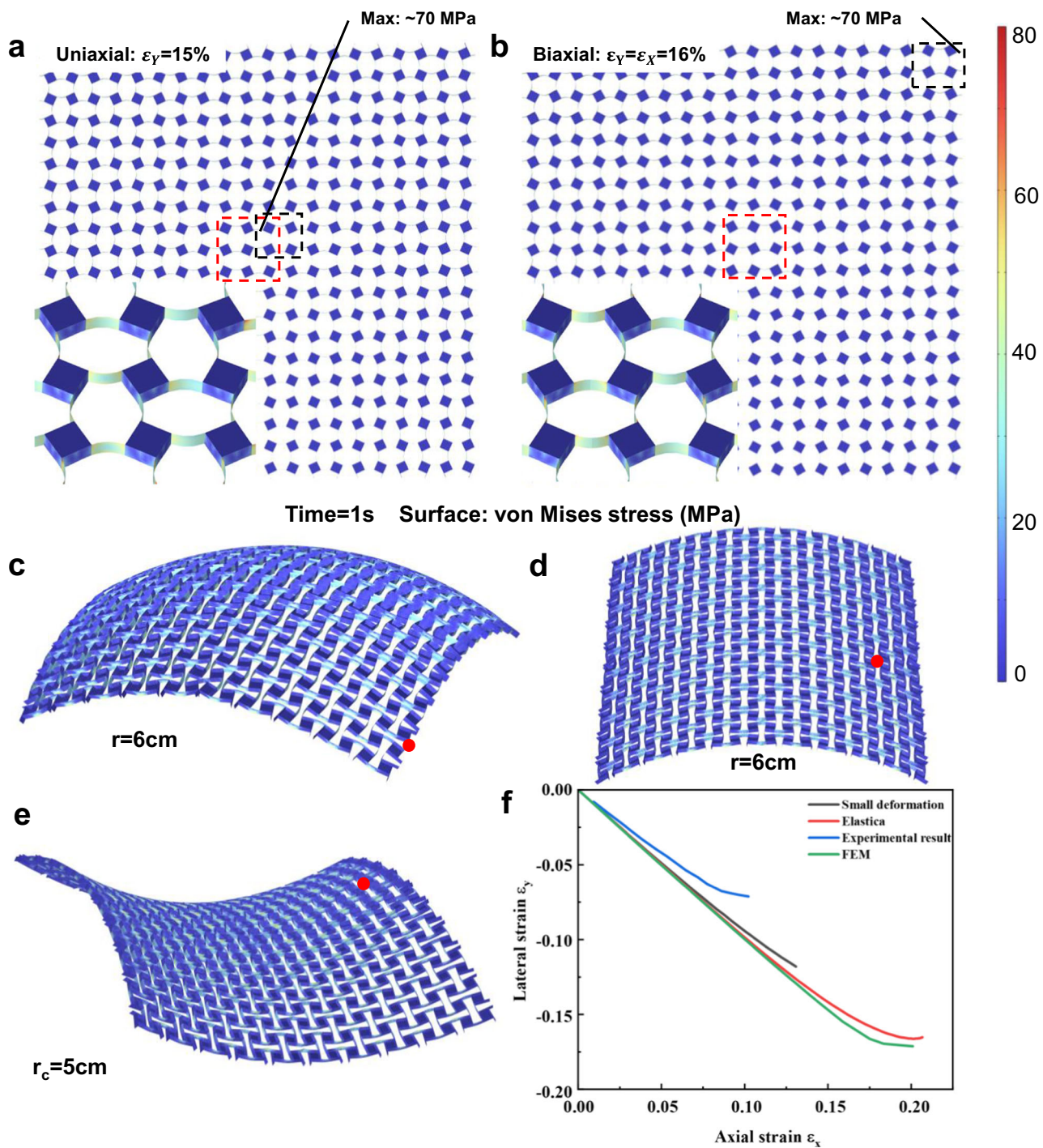


**Fig. 7 Stress distribution calculated in FEM. a** Uniaxial tension **(b)** Biaxial tension. Stress distribution was calculated in FEM for **(c)** spherical, **(d)** cylindrical, and **(e)** saddle surfaces, respectively. **f** Lateral-strain-axial-strain curve.

elastica model, finite element method (FEM) result by COMSOL Multiphysics 5.4, and TPU experimental result. When the strain is less than 0.15, all four curves are in close agreement. However, under large deformations, both the elastica model and FEM result manifest a dramatic increase in stiffness while the small deformation model and TPU experimental only increase steadily. Due to limited production process, the length to thickness ratio of the TPU sample is higher than that of our FPCB, results in a weaker inextensibility. Therefore, the TPU result manifests a smoother hardening process.

Further, we conducted FEM calculation to investigate the behavior of the island-interconnect structure under different boundary conditions, including uniaxial and biaxial tension as well as covering spherical, cylindrical and saddle surfaces. To simplify the computational process, we use a reduced 1/4 model, effectively working with a  $10 \times 10$  pixels calculation configuration. Symmetric boundary conditions are imposed on the left and bottom boundaries, constraining both corresponding displacements and rotation in-plane. For different loading scenarios, we apply specific boundary for (1) extruded example: a displacement boundary condition is applied along the uniaxial direction on the

boundary of the extrusion. Out-of-plane rotations are constrained, and displacements outside the plane are also restricted; (2) overlying surface example: an energy penalty function is introduced to weakly constrain all pixels to move only along the overlying surface. Comparing with the original rotating-square structure which has only one degree of freedom (DOF) to rotate, this structure exhibits more complex morphology, with local irregular deformation to adjust to any boundary conditions (as shown in Fig. 7). Since the structure also has a Poisson's ratio close to one under uniaxial tension, its global configuration in Fig. 7a is quite similar to that of the original structure as shown in Fig. 1d, e. Also, the deformation of the structure is almost identical when subjected to uniaxial and biaxial tension, with the maximum strain on the vertical interconnects to be only  $\sim 3\%$  (as shown in the insets of Fig. 7a, b). Not only does the slender interconnect bring more DOFs in plane via bending, but it also endows the structure a potential to deform out-of-plane via warping. When the structure is forced to cover a curve surface (Fig. 7c–e), the vertical interconnects can deform themselves naturally to enable out-of-plane deformation, with a similar maximum stress (around 60–70 MPa, marked with red dots) compared to pure in-plane stretching. On the other side, the introduction of vertical interconnects has significantly addressed the stress concentration in the rotating-square structure, thereby greatly enhancing the yield and reliability of the device.

Finally, we present the lateral-strain-axial-strain curve under four different conditions as shown in Fig. 7f, including small deformation model, elastica model, FEM result and experimental result. Results show that when deformation is small and the gravity effect is excluded, the slope of the curve (i.e., Poisson's ratio) is exact  $-1$ , and all of the elastica model, FEM result and experiment manifest a nonlinear behavior after stretching to a certain extent.

## DATA AVAILABILITY

The data that support the plots in this paper and other findings of this study are available from the corresponding authors upon reasonable request.

Received: 8 August 2023; Accepted: 17 December 2023;

Published online: 06 January 2024

## REFERENCES

- Mukhopadhyay, S. C. Wearable sensors for human activity monitoring: a review. *IEEE Sens. J.* **15**, 1321–1330 (2015).
- Someya, T. & Amagai, M. Toward a new generation of smart skins. *Nat. Biotechnol.* **37**, 382–388 (2019).
- Wang, Y., Hu, S., Xiong, T., Yonga, H. & Lei, Q. Recent progress in aircraft smart skin for structural health monitoring. *J. Sagepub. com.* **21**, 2453–2480 (2022).
- Whitesides, G. M. Soft Robotics. *Angew. Chem. - Int. Ed.* **57**, 4258–4273 (2018).
- Laschi, C., Mazzolai, B. & Cianchetti, M. Soft robotics: Technologies and systems pushing the boundaries of robot abilities. *Sci. Robot.* **1**, eaah3690 (2016).
- Yin, R. et al. Wearable sensors-enabled human-machine interaction systems: from design to application. *Adv. Funct. Mater.* **31**, 2008936 (2021).
- Patel, S., Park, H., Bonato, P., Chan, L. & Rodgers, M. A review of wearable sensors and systems with application in rehabilitation. *J. Neuroeng. Rehabil.* **9**, 21 (2012).
- Polygerinos, P. et al. Soft robotics: review of fluid-driven intrinsically soft devices; manufacturing, sensing, control, and applications in human-robot interaction. *Adv. Eng. Mater.* **19**, 1700016 (2017).
- Koo, J. H., Kim, D. C., Shim, H. J., Kim, T. H. & Kim, D. H. Flexible and stretchable smart display: materials, fabrication, device design, and system integration. *Adv. Funct. Mater.* **28**, 1–23 (2018).
- Zhou, A., Wang, H., Zhang, Y. & Hu, C. Recent progress of flexible OLEDs for wearable devices. *Fiber Integr. Opt.* **41**, 1–25 (2022).
- Callens, S. J. P. & Zadpoor, A. A. From flat sheets to curved geometries: Origami and kirigami approaches. *Mater. Today* **21**, 241–264 (2018).
- Rovenski, V. Y. Differential geometry of curves and surfaces: a concise guide. *Differ. Geom. Curves Surfaces A Concise Guid.* **1**, 1–206 (2006).

## ACKNOWLEDGEMENTS

The authors would like to acknowledge the HKUST LED-FPD Technology R&D Center at Foshan for helping fabricate the samples. The authors greatly appreciate the financial support from the startup fund and the IGN17EG06 project from the Hong Kong University of Science and Technology, Research Grants Council of Hong Kong under the General Research Funds (Grant No. 16200919 and 16203321), the National Natural Science Foundation of China through Grant No. 11932009, and the Science, Technology, and Innovation Commission of Shenzhen Municipality through Grant No. ZDSYS20210623092005017.

## AUTHOR CONTRIBUTIONS

Y.D. designed experiments, fabricated the devices and drafted the manuscript, K.X. cooperated in the mathematical analysis, simulation and helped draft the manuscript, R.J. helped draft the manuscript, W.L. helped draft the manuscript and involved in developing the simulation, Y.C. rendered 3D pictures and designed the driver circuit, Y.L. analyzed the feasibility of the project and revised the manuscript, X.W. and Y.H. helped design experiments and Prof. H.Y. and Prof. W.H. guided device fabrication and theoretical analysis, revised the manuscript and checked it for final submission. All authors contributed to the article and approved the submitted version.

## COMPETING INTERESTS

The authors declare no competing interests.

## ADDITIONAL INFORMATION

**Supplementary information** The online version contains supplementary material available at <https://doi.org/10.1038/s41528-023-00291-y>.

**Correspondence** and requests for materials should be addressed to Wei Hong or Hongyu Yu.

**Reprints and permission information** is available at <http://www.nature.com/reprints>

**Publisher's note** Springer Nature remains neutral with regard to jurisdictional claims in published maps and institutional affiliations.



**Open Access** This article is licensed under a Creative Commons Attribution 4.0 International License, which permits use, sharing, adaptation, distribution and reproduction in any medium or format, as long as you give appropriate credit to the original author(s) and the source, provide a link to the Creative Commons license, and indicate if changes were made. The images or other third party material in this article are included in the article's Creative Commons license, unless indicated otherwise in a credit line to the material. If material is not included in the article's Creative Commons license and your intended use is not permitted by statutory regulation or exceeds the permitted use, you will need to obtain permission directly from the copyright holder. To view a copy of this license, visit <http://creativecommons.org/licenses/by/4.0/>.

© The Author(s) 2024